

This is the accepted manuscript made available via CHORUS. The article has been published as:

# Measurement of the $2^{+} \rightarrow 0^{+}$ ground-state transition in the $\beta$ decay of $^{20}\text{F}$

O. S. Kirsebom *et al.*

Phys. Rev. C **100**, 065805 — Published 24 December 2019

DOI: [10.1103/PhysRevC.100.065805](https://doi.org/10.1103/PhysRevC.100.065805)

# Measurement of the $2^+ \rightarrow 0^+$ ground-state transition in the $\beta$ decay of $^{20}\text{F}$

O. S. Kirsebom,<sup>1,2,\*</sup> M. Hukkanen,<sup>3</sup> A. Kankainen,<sup>3</sup> W. H. Trzaska,<sup>3</sup> D. F. Strömberg,<sup>4,5</sup> G. Martínez-Pinedo,<sup>5,4,†</sup> K. Andersen,<sup>1</sup> E. Bodewits,<sup>6</sup> B. A. Brown,<sup>7</sup> L. Canete,<sup>3</sup> J. Cederkäll,<sup>8</sup> T. Enqvist,<sup>9</sup> T. Eronen,<sup>3</sup> H. O. U. Fynbo,<sup>1</sup> S. Geldhof,<sup>3</sup> R. de Groote,<sup>3</sup> D. G. Jenkins,<sup>10</sup> A. Jokinen,<sup>3</sup> P. Joshi,<sup>10</sup> A. Khanam,<sup>3,11</sup> J. Kostensalo,<sup>3</sup> P. Kuusiniemi,<sup>9</sup> K. Langanke,<sup>5,4</sup> I. Moore,<sup>3</sup> M. Munch,<sup>1</sup> D. A. Nesterenko,<sup>3</sup> J. D. Ovejas,<sup>12</sup> H. Penttilä,<sup>3</sup> I. Pohjalainen,<sup>3</sup> M. Reponen,<sup>3</sup> S. Rinta-Antila,<sup>3</sup> K. Riisager,<sup>1</sup> A. de Roubin,<sup>3</sup> P. Schotanus,<sup>6</sup> P. C. Srivastava,<sup>13</sup> J. Suhonen,<sup>3</sup> J. A. Swartz,<sup>1</sup> O. Tengblad,<sup>12</sup> M. Vilen,<sup>3</sup> S. Vinals,<sup>12</sup> and J. Äystö<sup>3</sup>

<sup>1</sup>*Department of Physics and Astronomy, Aarhus University, DK-8000 Aarhus C, Denmark*

<sup>2</sup>*Institute for Big Data Analytics, Dalhousie University, Halifax, NS, B3H 4R2, Canada*

<sup>3</sup>*University of Jyväskylä, Department of Physics,  
P.O. Box 35, FI-40014, University of Jyväskylä, Finland*

<sup>4</sup>*Institut für Kernphysik (Theoriezentrum), Technische Universität Darmstadt,  
Schlossgartenstraße 2, 64289 Darmstadt, Germany*

<sup>5</sup>*GSI Helmholtzzentrum für Schwerionenforschung, Planckstraße 1, 64291 Darmstadt, Germany*

<sup>6</sup>*SCIONIX Holland B.V., Regulierenring 5, 3981 LA Bunnik, The Netherlands*

<sup>7</sup>*National Superconducting Cyclotron Laboratory, Michigan State University, East Lansing, Michigan 48824, USA*

<sup>8</sup>*Department of Physics, Lund University, SE-22100 Lund, Sweden*

<sup>9</sup>*University of Oulu, Oulu Southern Institute, FI-90014, Finland*

<sup>10</sup>*Department of Physics, University of York, York YO10 5DD, United Kingdom*

<sup>11</sup>*Aalto University, P.O. Box 11000, FI-00076 Aalto, Finland*

<sup>12</sup>*Instituto de Estructura de la Materia, CSIC, E-28006 Madrid, Spain*

<sup>13</sup>*Department of Physics, Indian Institute of Technology, Roorkee 247667, India*

(Dated: February 26, 2020)

We report the first detection of the second-forbidden, non-unique,  $2^+ \rightarrow 0^+$ , ground-state transition in the  $\beta$  decay of  $^{20}\text{F}$ . A low-energy, mass-separated  $^{20}\text{F}^+$  beam produced at the IGISOL facility in Jyväskylä, Finland, was implanted in a thin carbon foil and the  $\beta$  spectrum measured using a magnetic transporter and a plastic-scintillator detector. The  $\beta$ -decay branching ratio inferred from the measurement is  $b_\beta = [0.41 \pm 0.08(\text{stat}) \pm 0.07(\text{sys})] \times 10^{-5}$  corresponding to  $\log ft = 10.89(11)$ , making this one of the strongest second-forbidden, non-unique  $\beta$  transitions ever measured. The experimental result is supported by shell-model calculations and has significant implications for the final evolution of stars that develop degenerate oxygen-neon cores. Using the new experimental data, we argue that the astrophysical electron-capture rate on  $^{20}\text{Ne}$  is now known to within better than 25% at the relevant temperatures and densities.

## I. INTRODUCTION

Second-forbidden, non-unique  $\beta$  transitions ( $\Delta J = 2$ ,  $\Delta\pi = \text{no}$ ) typically have very small branching ratios, which makes their detection rather challenging. Only around 27 such transitions have been observed [1]. Measurements of the rates and shapes of forbidden  $\beta$  transitions provide insights into nuclear structure and occasionally also into astrophysical processes.

Recent studies have highlighted the importance of the second-forbidden, non-unique, electron-capture transition from the  $0^+$  ground state of  $^{20}\text{Ne}$  to the  $2^+$  ground state of  $^{20}\text{F}$  for the final evolution of stars of 7–11 solar masses that develop degenerate oxygen-neon cores [2–4]. The strength of the transition is, however, not well constrained, neither experimentally nor theoretically, making an experimental determination highly desirable. The strength may be determined from the branching ratio of the inverse  $2^+ \rightarrow 0^+$  transition in the  $\beta$  decay of  $^{20}\text{F}$

(Fig. 1), but this transition is not easily detected as it is masked by the much faster, allowed,  $2^+ \rightarrow 2^+$  transition to the first-excited state in  $^{20}\text{Ne}$ . Indeed, previous attempts to detect the  $2^+ \rightarrow 0^+$  transition have been unsuccessful [7–10] yielding a rough upper limit of  $\sim 10^{-5}$  on the branching ratio [10]. The  $\beta$ -decay endpoint energies for the ground-state and first-excited state transitions are 7.025 MeV and 5.391 MeV, respectively<sup>1</sup>, leaving a rather narrow energy window for the detection of the ground-state transition. Here, we report the first successful measurement of the second-forbidden, non-unique,  $2^+ \rightarrow 0^+$  transition in the  $\beta$  decay of  $^{20}\text{F}$ , present shell-model calculations which corroborate the experimental result, and determine the impact on the astrophysical electron-capture rate on  $^{20}\text{Ne}$ . The astrophysical implications for the evolution of stars of 7–11 solar masses are dealt with elsewhere [12].

\* Corresponding author: oliver.kirsebom@dal.ca

† g.martinez@gsi.de

<sup>1</sup> The endpoint energies are known to sub-keV precision [5, 38].

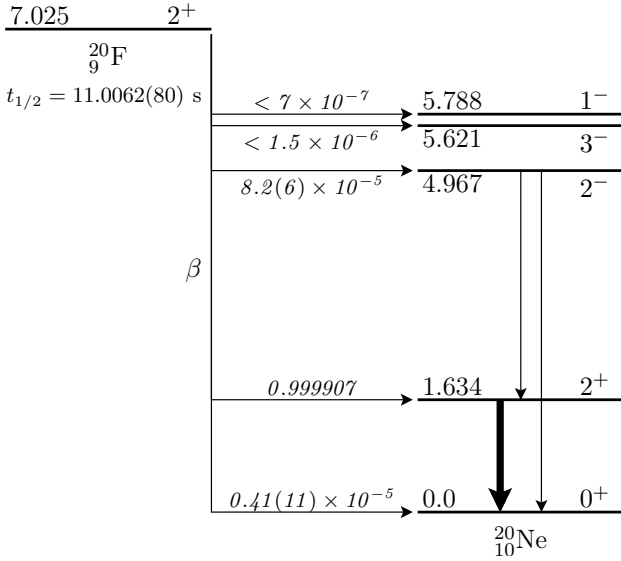


FIG. 1.  $^{20}\text{F}$   $\beta$ -decay scheme [5, 6] including the newly observed ground-state transition. The bold arrow indicates the  $\gamma$ -ray transition used for absolute normalisation. The branching ratios of the individual  $\beta$ -decay transitions are shown in italic. Energies are in MeV relative to the  $^{20}\text{Ne}$  ground state.

## II. EXPERIMENTAL SETUP

The experiment was performed at the IGISOL-4 facility of the JYFL Accelerator Laboratory in Jyväskylä, Finland [13, 14]. Radioactive ions of  $^{12}\text{B}^+$  and  $^{20}\text{F}^+$  were produced via  $(d, p)$  reactions on targets of boron (B) and barium fluoride ( $\text{BaF}_2$ ). The K130 cyclotron was used to produce the deuteron beam, which had an energy of 9 MeV and an intensity of around  $10 \mu\text{A}$ . For the production of the  $^{20}\text{F}^+$  ions, a  $53 \mu\text{m}$  thick tantalum (Ta) degrader was used to reduce the beam energy to 6 MeV. The B and  $\text{BaF}_2$  targets were  $0.5 \text{ mg/cm}^2$  and  $1.2 \text{ mg/cm}^2$  thick with backings of  $4.5 \mu\text{m}$  tantalum (Ta) and  $2 \mu\text{m}$  tungsten (W), respectively. The reaction products were thermalized in the IGISOL ion guide gas cell, using helium at a pressure of around 100 mbar for  $^{12}\text{B}$  and 250 mbar for  $^{20}\text{F}$ , and extracted with a sextupole ion guide [15]. After acceleration to 30 keV, the ions were separated based on their mass-to-charge ratio using a dipole magnet, before being guided to the experimental station where they were stopped in a thin ( $50 \mu\text{g/cm}^2$ ) carbon foil. The  $\beta$  spectrum of  $^{20}\text{F}$  was the primary interest of the experiment while the  $\beta$  spectrum of  $^{12}\text{B}$  provided important calibration data.

The detection system, shown in Fig. 2, consisted of a Siegbahn-Slätis type intermediate-image magnetic electron transporter [16] combined with an energy-dispersive detector. Such an arrangement is well suited for the measurement of rare ground-state transitions in nuclear  $\beta$  decays as the effective solid angle of the detector, and hence the count rate, is greatly increased by the focussing action of the magnetic field. Furthermore, and equally im-

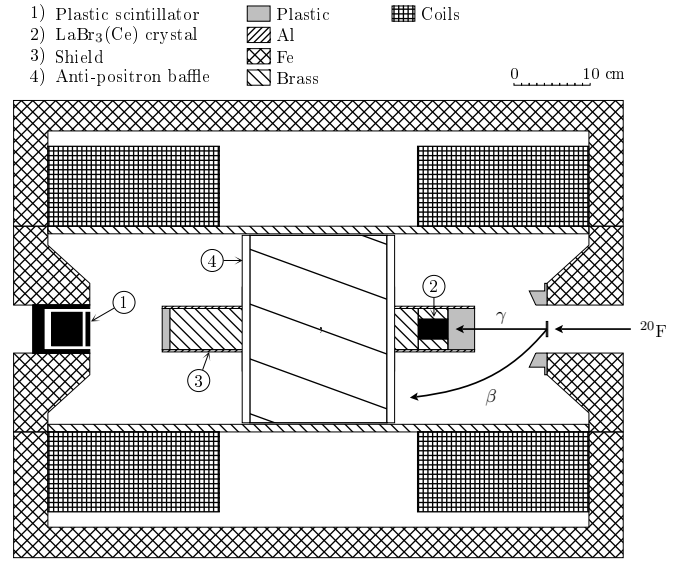


FIG. 2. Schematic diagram of the setup. The  $^{20}\text{F}$  beam comes in from the right and is stopped in the catcher foil. The 1.63-MeV  $\gamma$  ray is detected in the  $\text{LaBr}_3(\text{Ce})$  detector (2) that sits behind 3.5 cm of plastic, while the electron follows a helical path to the focal plane where it is detected in the plastic-scintillator detector (1).

portant, the shield on the centre axis prevents  $\gamma$  rays and electrons produced by transitions to excited states in the daughter nucleus from reaching the detector. This essentially eliminates  $\beta\gamma$  summing and  $\beta\beta$  pile-up as sources of background and leads to an improved sensitivity towards the ground-state transition.

The magnetic transporter was constructed at the Department of Physics, University of Jyväskylä (JYFL) in the 1980s [17], but has been fully refurbished for the present experiment. The  $\beta$  detector, shown in Fig. 3, has the shape of a cylinder and consists of a 5-mm thick outer detector, used as a veto against cosmic rays, and a  $45 \text{ mm} \times 45 \text{ mm}$  inner detector, used to measure the full energy of the electrons. The inner detector is further subdivided into a 5-mm thick front detector and a 40-mm thick main detector to provide additional discriminatory power. All three detectors (veto, front and main) are plastic scintillators read out with silicon photomultipliers. The detector dimensions represent a compromise between the requirement to fully stop a significant fraction of the most energetic electrons (the nominal range of 7-MeV electrons in plastic is 35 mm) and the requirement to minimize the cosmic-ray exposure.

Some of the calibration data presented in this paper were obtained using an earlier, two-channel version of the three-channel detector that we have just described. The two detectors have identical dimensions and only differ in one respect: the inner volume of the two-channel detector is not divided into a front and a main section. When necessary we use the labels v1 and v2 to distinguish between the two-channel (v1) and three-channel (v2) de-

tector. When no label is provided it is understood that the three-channel detector was used.

A small  $\text{LaBr}_3(\text{Ce})$  crystal placed inside the shield on the centre axis was used to detect the 1.63-MeV  $\gamma$  ray from the decay of  $^{20}\text{F}$ , thereby providing absolute normalisation of the  $\beta$  spectrum. Finally, a baffle placed at the centre of the magnet prevented positrons, which spiral in the opposite direction of electrons, from reaching the detector thereby eliminating positron emitters as a potential source of background, while reducing the electron flux by only 11%.

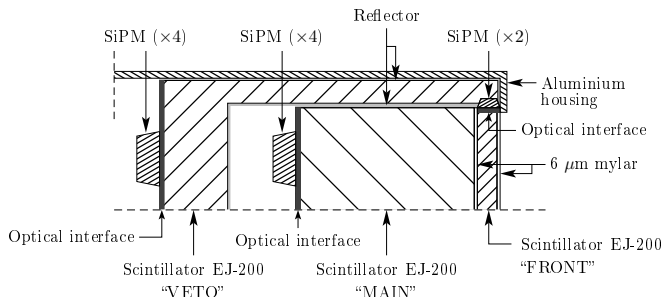


FIG. 3. Schematic diagram of plastic-scintillator detector. Built-in amplifiers and cables to the SiPMs are not shown. The dimensions (diameter  $\times$  length) of the plastic-scintillator volumes are:  $45 \times 5 \text{ mm}^2$  (FRONT),  $45 \times 40 \text{ mm}^2$  (MAIN) and  $55 \times 75 \text{ mm}^2$  (VETO). The other diameter of the aluminium housing is 60 mm.

### III. DATA ANALYSIS AND RESULTS

#### A. Characterization of the $\beta$ response

By only allowing electrons within a relatively narrow energy band to reach the detector, the magnetic transporter effectively “carves out” a slice of the  $\beta$  spectrum. This is demonstrated in Fig. 4, which shows energy spectra measured at three different magnetic-field strengths. The central energy selected by the magnetic transporter is approximately given by  $\bar{E}_\beta \simeq 7.72\tilde{I} + 3.01\tilde{I}^2 \text{ MeV}$ , where  $\tilde{I}$  is the electrical current expressed as a fraction of the maximum current provided by the power supply (700 A). The spectra obtained at  $\tilde{I} = 35.3\%$  and  $56.4\%$  show a central slice and the upper end of the allowed  $\beta$  spectrum of  $^{20}\text{F}$ , respectively. The spectra obtained at  $67.0\%$  and  $79.0\%$  show slices of the  $\beta$  spectrum of  $^{12}\text{B}$ , which has an end-point energy of 13.37 MeV. In all cases, the main peak is well reproduced by the GEANT4 simulation. Deviations occur in the low-energy tails, especially for the spectra obtained at the higher current settings, but these deviations are not important for the present analysis. The  $^{20}\text{F}$  spectra have been cleaned by requiring that no coincident signal is recorded in the veto detector (veto cut) and that the energy deposited in the front detector is between 0.65–1.60 MeV (front cut). The  $^{12}\text{B}$  spectra have also been subject to the veto cut, but

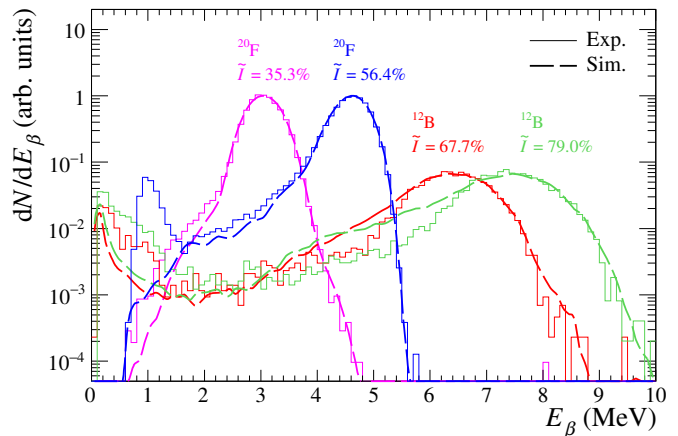


FIG. 4. Comparison of experimental and simulated energy spectra obtained at 35.3%, 56.4% ( $^{20}\text{F}$ ), 67.7% and 79.0% ( $^{12}\text{B}$ ) of the maximum electrical current. The  $^{20}\text{F}$  data have been subject to both veto and front cut, while the  $^{12}\text{B}$  data have been subject only to the veto cut.

the front cut could not be applied to these spectra because the  $^{12}\text{B}$  measurements were performed with the two-channel  $\beta$  detector.

The  $^{20}\text{F}$  and  $^{12}\text{B}$  data (only a subset of which are shown in Fig. 4) and data obtained with a calibrated  $^{207}\text{Bi}$  source, have been used to validate the absolute accuracy of the GEANT4 simulations all the way up to  $\bar{E}_\beta = 8.0 \text{ MeV}$ . As shown in Fig. 5, the simulated and experimental  $\beta$  transmission efficiencies exhibit reasonable agreement across the full energy range, with the simulation overestimating the transmission efficiency by 8% on average. The transmission efficiency is determined as  $\varepsilon_\beta = N_\beta N_\gamma^{-1} \varepsilon_\gamma$ , where  $N_\beta$  is the number of counts in the full-energy peak in the uncleaned  $\beta$  spectrum (*i.e.* before application of the veto and front cuts),  $N_\gamma$  is the number of 1.63-MeV  $\gamma$  rays, and  $\varepsilon_\gamma$  is the  $\gamma$ -ray detection efficiency, cf. Sec. IIID. We note that the overall normalization of the  $^{12}\text{B}$  data points could not be established experimentally due to the lack of a sufficiently intense  $\gamma$ -ray line. However, by monitoring the  $\beta$  count rate we were able to establish that the implantation rate was constant throughout the measurements, implying that the data points share the same overall normalization; its value was determined via a  $\chi^2$  fit to the data. The 8% overestimation may partly or entirely be attributed to the uncertainty on the  $\gamma$ -ray detection efficiency, which causes a 5% uncertainty on the normalization of the experimental transmission efficiency, cf. Sec. IIID.

On the other hand, the large scatter in the experimental data points observed in Fig. 5 may be attributed to temporal variations in beam optics, which affect the source geometry and hence the transmission efficiency. The occurrence of such temporal variations is evident in Fig. 6, which shows the transmission efficiency obtained in nine separate runs performed at the same magnetic-field strength ( $\tilde{I} = 35.3\%$ ) at different times during the

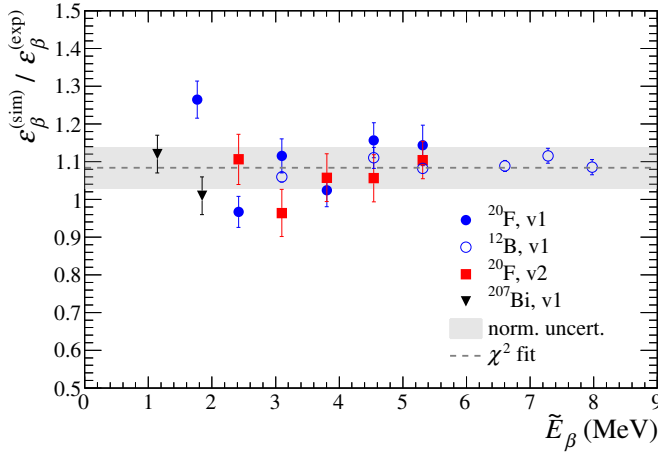


FIG. 5. Ratio of simulated and experimental transmission efficiencies,  $\varepsilon_{\beta}^{(\text{sim})}/\varepsilon_{\beta}^{(\text{exp})}$ , versus the central energy selected by the magnetic transporter,  $\tilde{E}_{\beta}$ . The data are labeled by the isotope ( $^{12}\text{B}$ ,  $^{20}\text{F}$ ,  $^{207}\text{Bi}$ ) and the detector (v1, v2) used for the measurement. The gray band indicates the systematic uncertainty on the normalization of the  $^{20}\text{F}$  data. The dashed line was obtained from a  $\chi^2$  fit to the data in which the normalization of the  $^{12}\text{B}$  data was allowed to vary freely (see text for details).

experiment. The temporal variations amount to a 13% spread in transmission efficiency, which we include as a systematic uncertainty on the final result.

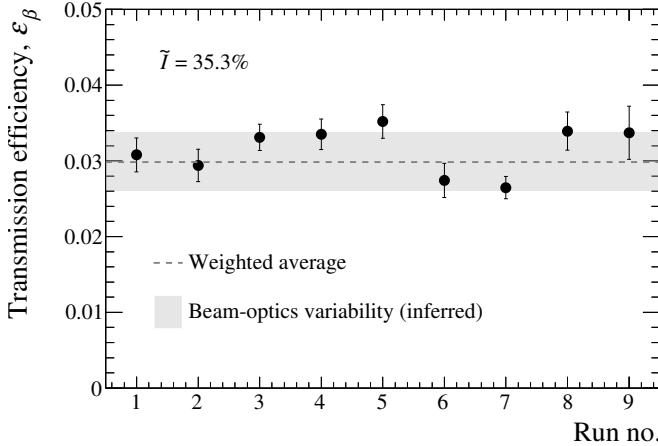


FIG. 6.  $\beta$  transmission efficiency obtained in nine separate runs performed at a magnetic-field strength of  $\tilde{I} = 35.3\%$  at different times during the experiment. The gray band indicates the spread attributed to variations in beam optics.

Finally, we examine the cut acceptance,  $\eta$ , defined as the fraction of counts in the full-energy peak that survive the veto and front cuts. As shown in Fig. 7, the simulation tends to overestimate the cut acceptance, partly due to the presence of cross-talk between the inner and the outer detectors, but also due to inaccuracies in the modeling of the stopping process in the detector volumes. The factor by which the simulation overestimates the cut

acceptance is small for  $\tilde{E}_{\beta}$ , but grows with increasing energy reaching 1.25(9) at  $\tilde{E}_{\beta} \sim 6.0$  MeV.

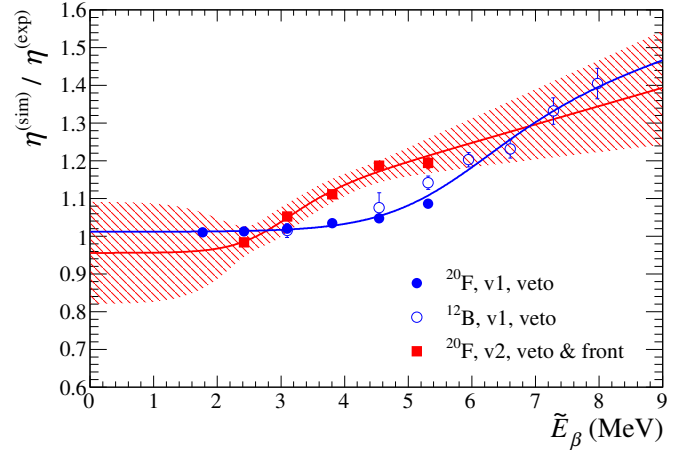


FIG. 7. Ratio of simulated and experimental cut acceptances,  $\eta^{(\text{sim})}/\eta^{(\text{exp})}$ , versus the central energy selected by the magnetic transporter,  $\tilde{E}_{\beta}$ . The data are labeled by the isotope ( $^{12}\text{B}$ ,  $^{20}\text{F}$ ,  $^{207}\text{Bi}$ ) and the detector (v1, v2) used for the measurement, and the cuts applied in the data analysis (veto & front). The solid lines and the hatched area show trend lines and the estimated uncertainty, respectively.

In Table I we summarize the sources of systematic uncertainty affecting the normalization of the  $\beta$  spectrum. In each case we give the estimated correction factor to the normalization of the GEANT4 simulation at  $\tilde{E}_{\beta} \sim 6.0$  MeV and the estimated uncertainty.

TABLE I. Sources of systematic uncertainty in the normalization of the experimental  $\beta$  spectrum. In each case, we give the correction factor by which the spectrum has been multiplied (second column) and the uncertainty on this factor (third column). The total uncertainty was obtained by adding the individual contributions in quadrature.

Source of sys. uncert.	Corr. factor	Uncert.
$\gamma$ -ray detection efficiency	1	5%
$\beta$ transmission efficiency	1/1.08	13%
cut acceptance	1/1.25	7%
total	1/1.35	16%

## B. Long-duration measurements

Long-duration measurements were performed at the current settings  $\tilde{I} = 67.7\%$  (67 h) and 70.5% (38 h) to search for a signal in the energy region 5.4–7.0 MeV, and at 79.0% (37 h) to demonstrate that any signal detected at the two lower settings did not persist above 7.0 MeV. The average  $^{20}\text{F}$  implantation rate for these measurements was 11 kHz, while the  $\gamma$  and  $\beta$  count rates were at most a few tens of Hz and a few Hz, respectively, im-

plying negligible dead time. Additionally, background data were collected at 67.7% and 70.5% for a total of 183 h. The  $\beta$  spectrum obtained at 67.7% is shown in Fig. 8. The cosmic-ray background dominates the raw

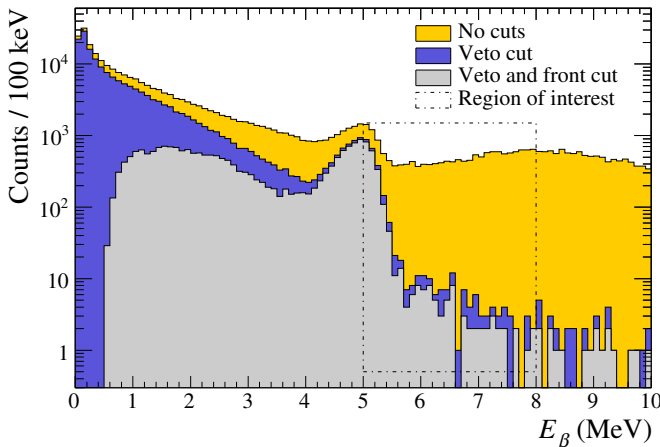


FIG. 8.  $\beta$  spectrum with cuts (gray) and without (yellow) obtained in the inner plastic-scintillator detector at 67.7% of the maximum electrical current. The dashed box indicates the region used for the likelihood fits shown in Fig. 11.

$\beta$  spectrum above 5.4 MeV while electrons from the allowed  $2^+ \rightarrow 2^+$  transition produce the bump centered at 5.0 MeV and the continuum below it. In the signal region the cosmic-ray background is reduced by a factor of 100 by the veto cut. The front cut removes another factor of 3.5 resulting in an overall reduction factor of 350. On the other hand, about 2/3 of the  $\beta$  particles survive the cuts, a fraction which would have been even larger in the absence of cross-talk between the inner and outer detectors.

### C. Investigation of the residual background

Below 3 MeV,  $\gamma$  rays, chiefly from the decays of  $^{40}\text{K}$  and  $^{208}\text{Tl}$ , are the main source of background, while cosmic-ray muons dominate above this energy, resulting in a background rate of 150 counts/h in the signal region (5.8–6.8 MeV). Measurements performed at different times of the year and different locations within the laboratory verified that this rate was very nearly constant to within a few percent. The residual background rate in the signal region after application of the veto cut was 1–2 counts/h. The energy dependence of the residual background is markedly different from the energy dependence of the raw background, indicating a different physical origin. In order to further characterize the residual background, a background measurement was performed at Callio Lab in the Pyhäsalmi mine in Pyhäjärvi, Finland, at the depth of 1430 meters (4100 m.w.e.) where the cosmic-ray muon flux is greatly suppressed [18]. In Fig. 9 we compare the spectrum obtained underground to a spectrum obtained at the surface. This compari-

son clearly demonstrates that the residual background is cosmic-ray induced. We note that the  $^{222}\text{Rn}$  room back-

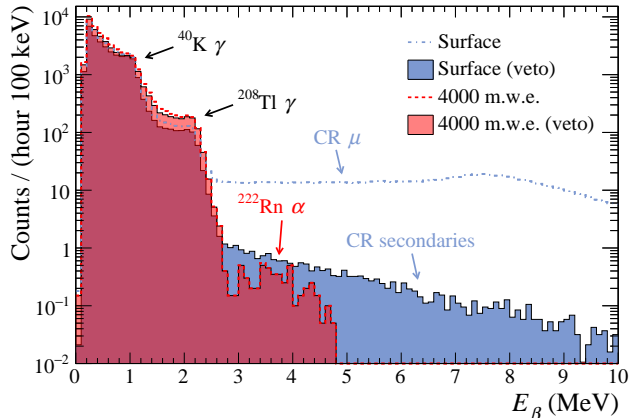


FIG. 9. The duration of the surface and underground measurements were 189 h and 20 h, respectively. The broad peaks at 1.0 MeV and 2.2 MeV are the Compton shoulders of the 1.46-MeV and 2.61-MeV  $\gamma$ -ray lines due to the naturally occurring radioactive isotopes  $^{40}\text{K}$  and  $^{208}\text{Tl}$  ( $^{232}\text{Th}$  decay chain). The broad peak centered at 3.8 MeV is produced by the 5.49-MeV  $\alpha$  particles from the decay of  $^{222}\text{Rn}$ , which lose a minimum of 0.66 MeV in the 6- $\mu\text{m}$  Mylar window of the  $\beta$  detector before entering the scintillation volume, plus any energy loss in the air *en route* to the detector.

ground activity at Callio Lab is ten times higher than at the JYFL laboratory (200 vs. 20 Bq/m<sup>3</sup>), which explains the enhanced  $^{222}\text{Rn}$   $\alpha$  peak in the underground spectrum. Additional measurements performed at the surface with the detector fully shielded on all sides by 5 cm of lead further showed that  $\gamma$  rays cannot be the main component of the residual background. We therefore conclude that hadronic secondaries, and neutrons in particular, from cosmic-ray interactions in the atmosphere and the roof of the laboratory are the likely source of the residual background. Finally, we note that placing the detector inside the magnetic transporter had little or no effect on the residual background. Similarly, the magnetic field seemed to exert little or no influence on the residual background although changes at the level of 10% or below cannot be excluded.

### D. Absolute normalization

Returning to the long-duration  $^{20}\text{F}$  measurements, we show in Fig. 10 the  $\gamma$  spectrum obtained at 67.7%. The well-resolved 1.63-MeV line from the decay of  $^{20}\text{F}$ , which is used for absolute normalisation, is clearly visible. The efficiency of the  $\text{LaBr}_3(\text{Ce})$   $\gamma$ -ray detector at 1.63 MeV was determined online from the ratio of  $\beta\gamma$  coincidences and  $\beta$  singles events, yielding the value  $\varepsilon_\gamma = 0.59(3) \times 10^{-4}$ . This online calibration was confirmed by an offline calibration made using radioactive

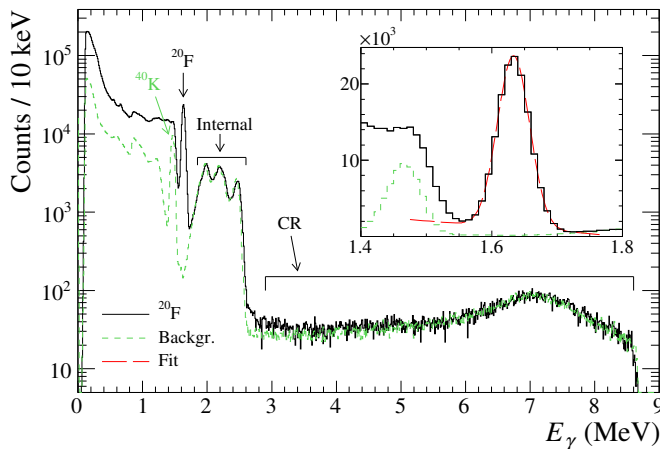


FIG. 10.  $^{20}\text{F}$   $\gamma$ -ray spectrum (solid, black line) and background  $\gamma$ -ray spectrum (short-dashed, green line) obtained in the  $\text{LaBr}_3(\text{Ce})$  detector at 67.7% of the maximum electrical current. The characteristic 1.63-MeV line of  $^{20}\text{F}$  sits between the 1.46-MeV background line due to  $^{40}\text{K}$  and the peaks at 1.8–2.6 MeV due to the internal activity of the  $\text{LaBr}$  crystal. Cosmic-ray muons dominate above 3 MeV. The inset shows a zoom-in on the 1.63-MeV line and the line-shape fit (long-dashed, red line).

sources of  $^{137}\text{Cs}$ ,  $^{207}\text{Bi}$ ,  $^{152}\text{Eu}$  and  $^{60}\text{Co}$  of known activities, which exhibit  $\gamma$ -ray lines with known relative intensities covering the energy range 0.3–1.8 MeV.

### E. Detection of the forbidden transition

Fig. 11 shows the cleaned  $\beta$  spectra obtained in the long-duration measurements, zoomed in on the region of interest. The spectra obtained at 67.7% and 70.5% reveal a clear excess of counts in the signal region when compared to the background spectrum. For example, the spectrum at 67.7% has  $55 \pm 7$  counts between 5.8–6.8 MeV while the background spectrum, downscaled to account for the longer measurement time, only has  $30 \pm 3$  counts in the same region. Equally important, no excess of counts is observed above the signal region in the data obtained at 79.0%. Based on the measurements performed at lower current settings (Fig. 8) we can exclude  $\beta\gamma$  summing and  $\beta\beta$  pile-up as possible explanations. Furthermore, the analysis of the temporal distribution of the counts between 5.8–6.8 MeV shown in Fig. 12 reveals a clear correlation with the  $^{20}\text{F}$  implantation rate, which varied by more than a factor of two during the experiment, while the temporal distribution of the counts above 7.0 MeV shows no such correlation. Thus, the observed signal is consistent with being due to the hitherto unobserved, second-forbidden, ground-state transition in the  $\beta$  decay of  $^{20}\text{F}$ .

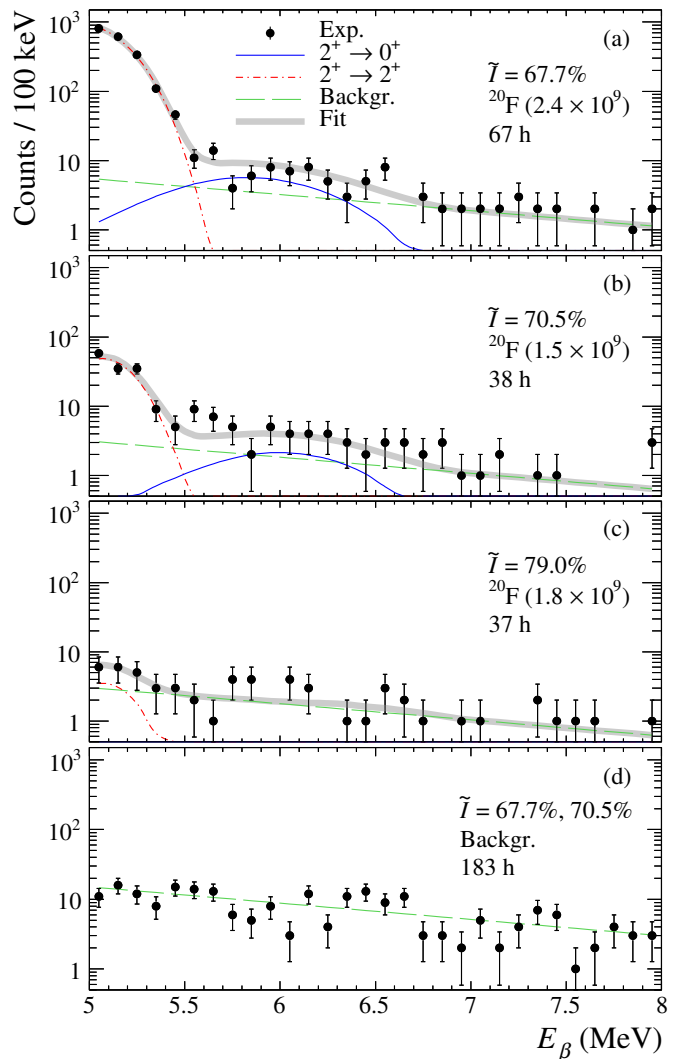


FIG. 11. Likelihood fits to the experimental data in the energy region 5.0–8.0 MeV obtained with beam (a–c) and without (d), at current settings focused on the region of interest (67.7% and 70.5%) and immediately above it (79.0%). The contribution of the second-forbidden, ground-state transition in the  $\beta$  decay of  $^{20}\text{F}$  is shown by the thin, solid (blue) curve.

## IV. BRANCHING RATIO

The previous section has provided evidence that the second forbidden transition connecting the ground states of  $^{20}\text{F}$  and  $^{20}\text{Ne}$  has been measured. In order to convert the signal observed between 5.8–6.8 MeV into a branching ratio and hence determine the magnitude of the matrix element, we must estimate the unobserved part of the forbidden  $\beta$  spectrum below 5.8 MeV, where the decay is dominated by the allowed transition. We do so guided by shell-model calculations as described in the following.



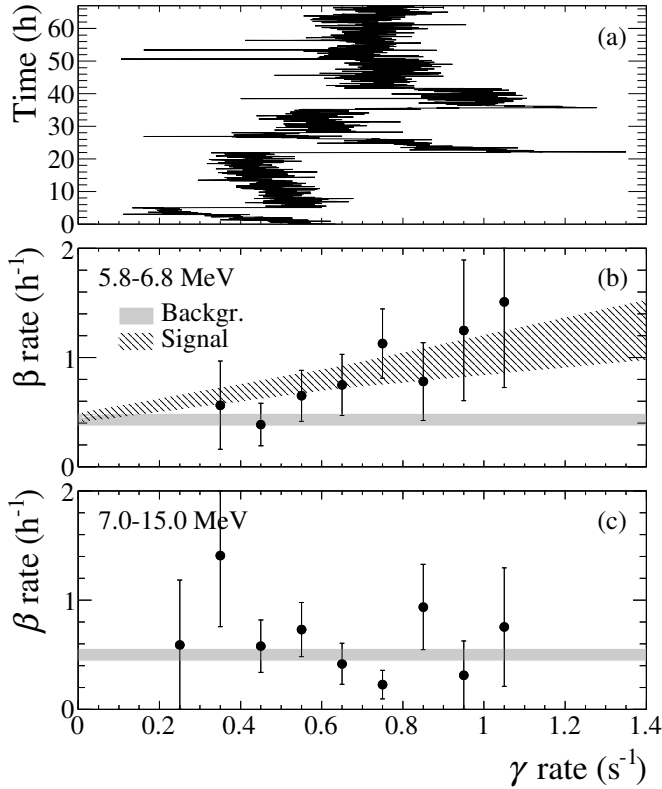


FIG. 12. (a) Temporal variations in  $\gamma$ -ray count rate during 67 hours of measurement at  $\tilde{I} = 67.7\%$ . (b) Correlation between  $\gamma$ -ray count rate and  $\beta$  count rate in the energy region  $E_\beta = 5.8\text{--}6.8$  MeV. (c) Same as (b) but for the energy region  $E_\beta > 7.0$  MeV.

### A. Shell-model calculations

For the calculation of the second-forbidden  $\beta$ -decay rate and  $\beta$  spectrum we follow the formalism of Behrens and Bühring [19]. This formalism accounts for the distortion of the electron wave function due to the nuclear charge, which leads to the appearance of additional matrix elements when compared to the formalism of Walecka [20, 21] used in Ref. [22].

The second-forbidden  $\beta$ -decay rate between the ground states of  $^{20}\text{F}$  and  $^{20}\text{Ne}$  can be expressed as

$$\lambda^{\beta^-} = \frac{\ln 2}{K} \int_1^q C(w) w p (q - w)^2 F(Z, w) dw$$

where  $w = (E_\beta + m_e c^2)/m_e c^2$  is the total electron energy in units of  $m_e c^2$ ,  $p = \sqrt{w^2 - 1}$  is the electron momentum in units of  $m_e c$ , and  $q = (M_p c^2 - M_d c^2)/(m_e c^2)$  is the energy difference between the initial and final nuclear state,  $M_p$  and  $M_d$  being the nuclear mass of the parent and daughter nucleus. The constant  $K = 6144 \pm 2$  s has been determined from superallowed Fermi transitions [23].  $F(Z, w)$  is the Fermi function, which arises due to the Coloumb interaction between the electron and the daughter nucleus with atomic number  $Z$ . Finally,  $C(w)$  is

the shape factor, which depends on the matrix elements of the transition. For the  $2^+ \rightarrow 0^+$  second-forbidden non-unique transition the shape factor has the form

$$C(w) = a_0 + \frac{a_{-1}}{w} + a_1 w + a_2 w^2 + a_3 w^3 + a_4 w^4$$

with the coefficients  $a_n$  given by combinations of seven matrix elements [19, 24].

TABLE II. Matrix elements determining the shape factor of the second-forbidden transition between the ground states of  $^{20}\text{F}$  and  $^{20}\text{Ne}$ . The second column shows the values obtained from a shell-model (SM) calculation with the USDB interaction. The third column shows the values obtained from a shell-model calculation in which the matrix elements have been constrained based on the conserved vector current (CVC) theory and the E2 strength of the decay of the isobaric analog state of  $^{20}\text{F}$  to the ground state of  $^{20}\text{Ne}$ . The quenched matrix elements can be obtained by multiplying the axial values by a factor  $1/g_A$ . (See text for additional information.)

Matrix element	SM	SM+CVC+E2
$V_{211}^0$	0	$-0.0118^a$
$V_{220}^0$	0.252	$0.184^a$
$V_{220}^0(1, 1, 1, 1)$	0.301	$0.220^a$
$V_{220}^0(2, 1, 1, 1)$	0.287	$0.210^a$
$A_{221}^0$	$-0.122$	$-0.122$
$A_{221}^0(1, 1, 1, 1)$	$-0.142$	$-0.142$
$A_{221}^0(2, 1, 1, 1)$	$-0.135$	$-0.135$

<sup>a</sup> Matrix elements constrained from experimental data

We have performed shell-model calculations in the  $sd$ -shell valence space using the USDB interaction [25] and the code NUSHELLX [26]. For the evaluation of the many-body matrix elements we use the single-particle matrix element expressions provided in Ref. [19] modified to account for the fact that our shell-model calculations follow the Condon-Shortley [27] phase convention instead of the Biedenharn-Rose phase convention [28]. The resulting matrix elements are shown in Table II. Our calculations use harmonic-oscillator single-particle wave functions with a radial parameter of  $b = 1.86$  fm and a uniform charge radius of  $R = 3.88$  fm. These values reproduce the root-mean-square radius of  $^{20}\text{Ne}$  determined from X-ray spectroscopy of muonic atoms [29]. Using Wood-Saxon wave functions instead of harmonic-oscillator wave functions, we obtain very similar matrix elements.

One limitation of our  $0\hbar\omega$   $sd$ -shell calculations is that the relativistic matrix element  $V_{211}^0$  is identically zero for harmonic-oscillator wave functions. This is not the case for Wood-Saxon wave functions, but the value obtained ( $V_{211}^0 = -0.004$ ) is too small to affect the results. Extending the model space to include multi- $\hbar\omega$  excitations is beyond the goals of the present publication and hence we follow a different approach to determine the  $V_{211}^0$  matrix element. Following Ref. [19] the conserved



vector current (CVC) theory provides a relationship between  $V_{F_{211}}^0$  and  $V_{F_{220}}^0$ ,

$$V_{F_{211}}^0 = -\frac{1}{\sqrt{10}} \left( \frac{E_\gamma R}{\hbar c} \right) V_{F_{220}}^0, \quad (1)$$

where  $E_\gamma = 10.273$  MeV is the excitation energy of the isobaric analog state of the ground state of  $^{20}\text{F}$  in  $^{20}\text{Ne}$  [30]. The CVC relation (1) is expected to hold for the “exact” matrix elements, but may break for matrix elements computed in a restricted model space using the impulse approximation as in our case. To quantify this effect we further relate the magnitude of the matrix element  $V_{F_{220}}^0$  to the experimentally determined E2 strength of the decay of the 10.273 MeV state to the ground state of  $^{20}\text{Ne}$  assuming isospin symmetry.

$$|V_{F_{220}}^0| = \frac{1}{R^2} \left( \frac{8\pi B(E2)}{e^2} \right)^{1/2}. \quad (2)$$

Adopting the experimental strength of  $B(E2) = 0.306(84) e^2 \text{ fm}^4$ , we obtain  $|V_{F_{220}}^0| = 0.184(25)$ , while the sign of the matrix element is determined based on the shell-model results. The matrix elements  $V_{F_{220}}^0(1, 1, 1, 1)$  and  $V_{F_{220}}^0(2, 1, 1, 1)$  contain a slightly different radial dependence than the factor of  $r^2$  appearing in  $V_{F_{220}}^0$ . We assume that the ratios  $V_{F_{220}}^0(1, 1, 1, 1)/V_{F_{220}}^0$  and  $V_{F_{220}}^0(2, 1, 1, 1)/V_{F_{220}}^0$  are well described by the shell-model calculations. The full set of matrix elements

obtained in this way are listed in the column labeled “SM+CVC+E2” in Table II.

The axial matrix elements  $A_{F_{221}}^0$ ,  $A_{F_{221}}^0(1, 1, 1, 1)$ , and  $A_{F_{221}}^0(2, 1, 1, 1)$  could be affected by the quenching of the axial coupling constant observed in Gamow-Teller decays, see e.g. Ref. [31]. However, previous studies have not shown conclusive evidence that such a quenching is also present in non-unique second-forbidden transitions [32–34]. Hence, we will consider in the following two different cases using either the bare value of  $g_A = -1.27$  or the quenched value  $g_A = -1.0$ . The numbers in table II have been obtained for  $g_A = -1.27$ .

In Fig. 13 we show the shape factor and  $\beta$  spectrum of the second forbidden transition as a function of the electron kinetic energy. The theoretical  $\log ft$  values for the different cases are shown in the last column of Table III. Looking at the shape factor and  $\beta$  spectrum one can notice important differences between the purely theoretical results, labeled “SM”, and those constrained by experimental information, labeled “SM+CVC+E2”. In the former case the shape is slightly distorted towards low energies compared with the allowed shape while in the latter case it is quite distorted towards high energies. This distortion originates from the important contribution of the relativistic matrix element  $V_{F_{211}}^0$  to the  $w, w^2$  and  $w^3$  terms that dominate the shape factor at high energies. For energies around the allowed  $Q$ -value,  $w = 5.391/0.511 + 1 = 11.55$ , the shape factor can be expressed as,

$$C(11.55) = 1.3 \times 10^{-6} \left[ (A_{F_{221}}^0)^2 + 58.75 A_{F_{221}}^0 V_{F_{211}}^0 + 1231 (V_{F_{211}}^0)^2 + 1.405 A_{F_{221}}^0 V_{F_{220}}^0 + 81.08 V_{F_{211}}^0 V_{F_{220}}^0 + 1.777 (V_{F_{220}}^0)^2 \right] \quad (3)$$

where the ratios  $V_{F_{KLs}}^0(k_e, 1, 1, 1)/V_{F_{KLs}}^0$  have been obtained from the shell-model calculations. One can see the important role of the relativistic matrix element  $V_{F_{211}}^0$  in determining the shape factor at high energies. For the two limiting cases considered above we have,

$$C(11.55) = 1.3 \times 10^{-6} \begin{cases} (A_{F_{221}}^0)^2 + 1.405 A_{F_{221}}^0 V_{F_{220}}^0 + 1.777 (V_{F_{220}}^0)^2, & V_{F_{211}}^0 = 0 \\ (A_{F_{221}}^0)^2 - 2.346 A_{F_{221}}^0 V_{F_{220}}^0 + 1.619 (V_{F_{220}}^0)^2, & V_{F_{211}}^0 \text{ from Eq. (1)} \end{cases} \quad (4)$$

From the relative signs of the vector and axial matrix elements given in Table II, their interference is destructive for the first case and constructive in the second case. Furthermore, quenching leads to an small enhancement of the shape factor in the first case and a larger reduction in the second case.

As an additional validation of our theoretical approach, we have also computed the shape factor using a more general formalism that includes next-to-leading-order nuclear-matrix elements [35]. We find that these additional matrix elements have negligible influence on the shape factor of the forbidden transition.

In the next section, we combine the theoretical shape factors with the experimental  $\beta$  spectrum to determine

the branching ratio of the forbidden transition.

## B. Likelihood fits to the experimental $\beta$ spectrum

In order to determine the branching ratio, we perform a likelihood fit to the experimental  $\beta$  spectrum between 5.0–8.0 MeV, in which we allow the normalisation of the simulated spectra of the allowed and forbidden transitions to vary freely, while the background is modelled by a simple exponential function with two free parameters. While the normalisation of the allowed transition is, in principle, fixed, in practice it is necessary to allow the normalisation to vary because the GEANT4 simu-

TABLE III. Effect of the adopted shape factor on the fit quality and the inferred branching ratio and  $\log ft$  value of the forbidden transition. We use the following notation: SM: Shell-model calculation; CVC+E2: Non-zero relativistic matrix element inferred from the CVC relation using the experimental E2 strength. The theoretically preferred shape factor is indicated in bold font. The fits with and without the forbidden transition have  $N = 112$  and  $113$  degrees of freedom, respectively. For the branching ratio ( $b_\beta$ ) we give the statistical fit uncertainty first, followed by the systematic experimental uncertainty; these are added in quadrature, including also the (significantly smaller) uncertainties on the end-point energy and the total half-life, to obtain the final uncertainty on the  $\log ft$  value.

Forbidden transition	Shape	$g_A$	$\chi^2/N$	$p$ -value	$b_\beta (\times 10^{-5})$	$\log ft$	$\log ft$ (theory)
yes	<b>SM+CVC+E2</b>	<b>-1.27</b>	<b>1.193</b>	<b>0.080</b>	<b>0.41(8)(7)</b>	<b>10.89(11)</b>	<b>10.86</b>
yes	SM+CVC+E2	-1.0	1.190	0.083	0.43(8)(7)	10.88(11)	10.91
yes	SM	-1.27	1.190	0.083	0.90(17)(14)	10.55(11)	10.76
yes	SM	-1.0	1.189	0.083	0.95(18)(15)	10.53(11)	10.73
yes	allowed	-	1.192	0.081	1.10(21)(18)	10.46(11)	-
no	-	-	1.518	0.00032	0	-	-

TABLE IV. Quality of the likelihood fits to the spectra in Fig. 11 performed with the theoretically preferred forbidden shape factor (“yes”) and assuming no contribution from the forbidden transition (“no”).

Panel	Forbidden transition					
	yes			no		
	$N$	$\chi^2/N$	$p$ -value	$N$	$\chi^2/N$	$p$ -value
(a)	24	1.39	0.098	25	1.97	0.0027
(b)	24	1.35	0.12	25	1.79	0.0087
(c)	24	1.08	0.35	25	1.05	0.39
(d)	28	1.50	0.044	28	1.82	0.0049
all	112	1.19	0.080	113	1.52	0.00032

lation becomes inaccurate in the low-energy tail of the transmission window. We also allow for a small ( $< 50$  keV) constant energy shift to account for inaccuracies in the energy calibration.

We perform such a likelihood fit for each of the four forbidden shape factors shown in Fig. 13. For reference, we also perform fits assuming a forbidden shape factor of unity (*i.e.* allowed shape) and assuming no contribution from the forbidden transition. The results of these fits are summarized in Table IV. Apart from the fit that ignores the contribution of the forbidden transition, all fits have practically identical fit qualities, implying that the shape factor is essentially unconstrained by the experimental data. As a result, the branching ratios differ substantially, ranging from  $\sim 0.4 \times 10^{-5}$  to  $\sim 1.0 \times 10^{-5}$ , with the smaller value being favored by the theoretical arguments given in Sec. IV B. We note that our result is consistent with the existing upper limit of  $\sim 10^{-5}$ , which was obtained assuming an allowed shape [10].

When comparing the theoretical and experimental  $\log ft$  values we find that the theoretical  $\log ft$  values constrained by experimental data, labeled “SM+CVC+E2”, are consistent with experimental  $\log ft$  values, while the purely theoretical  $\log ft$  values, labeled “SM”, overesti-

mate the half-life of the forbidden transition by a factor of  $\sim 1.6$ . We do not find major differences between the quenched and unquenched cases. In the following, we will adopt the shape factor given by the unquenched “SM+CVC+E2” model, shown in boldface in Table III, as this model is consistent with all the available experimental data including the CVC theory, the strength of the analog E2 decay in  $^{20}\text{Ne}$ , and the presently measured forbidden  $\beta$  spectrum, and there is no compelling evidence supporting the need of quenching for second forbidden transitions [32, 33].

Adopting this forbidden shape factor, the simultaneous fit to the four spectra shown in Fig. 11 yields a branching ratio of  $0.41(8) \times 10^{-5}$  and a goodness of fit of  $\chi^2/N = 133.6/112 = 1.193$  corresponding to an acceptable  $p$ -value of  $P_{\chi^2 > 133.6} = 0.080$ . If, on the other hand, we fix the branching ratio to zero, the goodness of fit worsens to  $\chi^2/N = 171.5/113 = 1.52$  corresponding to a  $p$ -value of only  $P_{\chi^2 > 171.5} = 0.00032$ , providing clear evidence for a positive observation.

In Fig. 14 we show the dependence of the goodness of fit on the assumed end-point energy of the forbidden transition. The best fit is obtained by adopting an end-point energy very close to the actual value of 7.025 MeV. The 95% confidence interval is determined to be [6.74; 8.00] making it highly unlikely that an unknown  $\beta^-$ -unstable beam contaminant should be the cause of the observed signal. This is in accordance with expectations as  $^{20}\text{F}$  is the only  $\beta$  emitter with mass 20 produced by the  $^{19}\text{F}(d, p)$  reaction at 6 MeV. Measurements performed on neighboring masses and on mass 40 were used to rule out the possibility that the signal was due to a  $\beta$  emitter with a mass different from 20, transmitted to the setup through the tails of the acceptance window of the dipole magnet or as doubly-charged ions.

Taking into account the uncertainties related to the normalisation of the  $\beta$  spectrum discussed above, our result for the branching ratio of the forbidden transition is  $b_\beta = [0.41 \pm 0.08(\text{stat}) \pm 0.07(\text{sys})] \times 10^{-5}$ . This translates into  $\log ft = 10.89(11)$ , where the statistical and

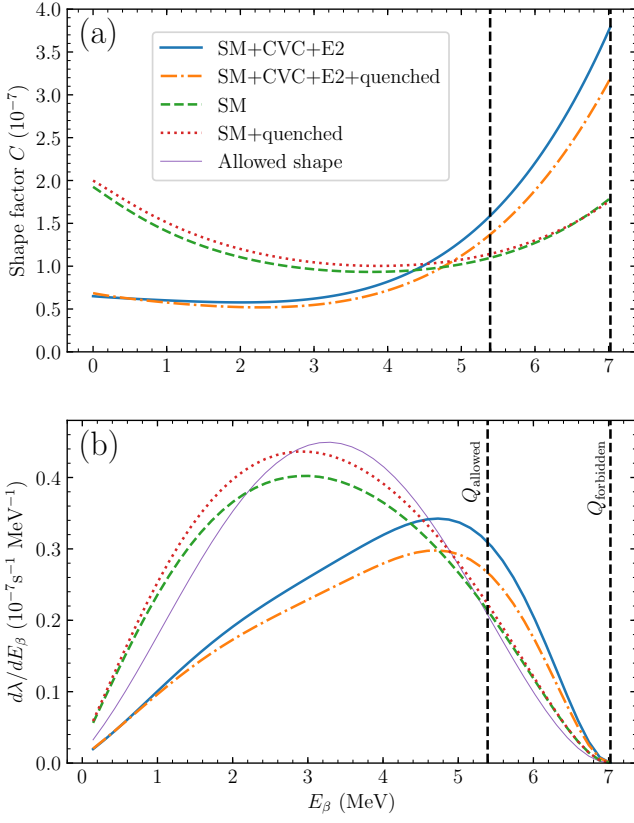


FIG. 13. Theoretical shape factor (a) and  $\beta$  spectrum (b) for the second forbidden transition as a function of the electron kinetic energy for the different cases discussed in text and table II. The dashed vertical lines indicate the end-point energies of the allowed ( $Q_{\text{allowed}}$ ) and forbidden ( $Q_{\text{forbidden}}$ ) transition, respectively. The thin violet line shows the allowed spectral shape arbitrarily normalized to the “SM” case.

systematical uncertainty have been added in quadrature.

## V. ELECTRON CAPTURE RATE

The astrophysical importance of the forbidden transition was first pointed out in Ref. [2], where it was argued that the inverse  $0^+ \rightarrow 2^+$  transition could enhance the rate of electron capture on  $^{20}\text{Ne}$  in dense and hot astrophysical environments, thereby affecting the final evolution of stars that develop degenerate cores of oxygen and neon. Ref. [2] also provided an estimate of the electron-capture rate based on the previous upper limit on the branching ratio of the forbidden transition [10] assuming an allowed shape. In the following, we generalize the calculation of the electron-capture rate to account for the forbidden shape.

At the high densities and temperatures of a degenerate oxygen-neon stellar core the nuclei are fully ionized and the electrons form a relativistic and degenerate Fermi gas. The energy of the electrons follow the Fermi-Dirac

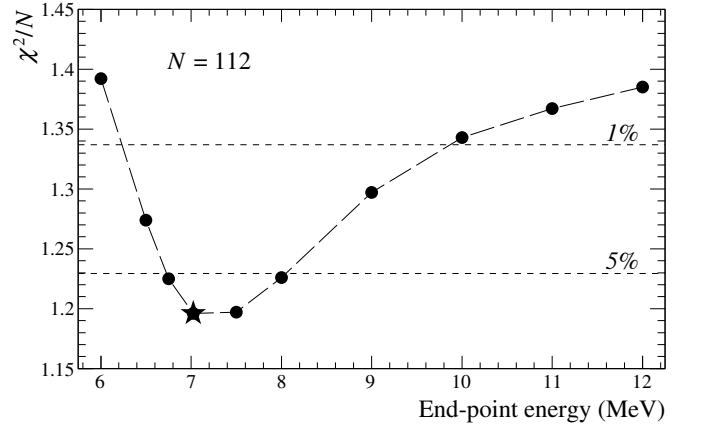


FIG. 14. Dependence of the goodness of fit on the assumed end-point energy of the forbidden transition. The 5% and 1% significance levels are shown by the dashed horizontal lines. The actual end-point energy of 7.025 MeV is indicated by the star.

distribution with chemical potential  $\mu_e$  related to  $\rho Y_e$ , where  $\rho$  denotes the matter density and  $Y_e$  the electron fraction. The electron capture rate via the forbidden transition is given by,

$$\lambda^{EC} = \frac{\ln 2}{K} \int_q^\infty C(w) w p(w - q)^2 F(Z, w) S_e(w, \mu_e) dw \quad (5)$$

where  $q$  is the positive  $Q$ -value of the transition in units of the electron mass,  $S_e(w, \mu_e)$  the Fermi-Dirac distribution, and  $F(Z, w)$  is the Fermi function, where  $Z$  is the charge number of the capturing nucleus. Screening corrections have been included in the calculation of the rate following Refs. [2, 36].

We compute the shape factor of the electron-capture transition using the same expression as for  $\beta$  decay, taking into account the different kinematics ( $E_\nu = Q - E_e$  for  $\beta^-$  decay and  $E_\nu = E_e - Q$  for electron capture), using the same relative phases of the matrix elements as in Table II, and correcting for the trivial factor of  $\sqrt{5}$  arising from the reversal of initial and final spins.

Fig. 15 shows the shape factors and  $\beta$  spectra for the various cases considered including the assumption of allowed shape. In all cases, the shape factors have been normalized to the experimental  $ft$  value by multiplying all matrix elements by a constant factor. This factor is very close to 1 for the experimentally constrained matrix elements, labeled “SM+CVC+E2”, and close to 0.7 for the purely theoretical matrix elements, labeled “SM”. Above the end point of the forbidden transition ( $E_\beta > Q_{\text{forbidden}}$ ), we show the shape factor of electron capture and the electron-capture rate computed for the representative conditions of temperature  $\log_{10} T(\text{K}) = 8.6$  and density  $\log_{10} \rho Y_e (\text{g cm}^3) = 9.6$ . In the region between the end points of the allowed and forbidden transitions ( $Q_{\text{allowed}} < E_\beta < Q_{\text{forbidden}}$ ), the  $\beta$  spectra are very similar once normalized to the experimental data. The ex-

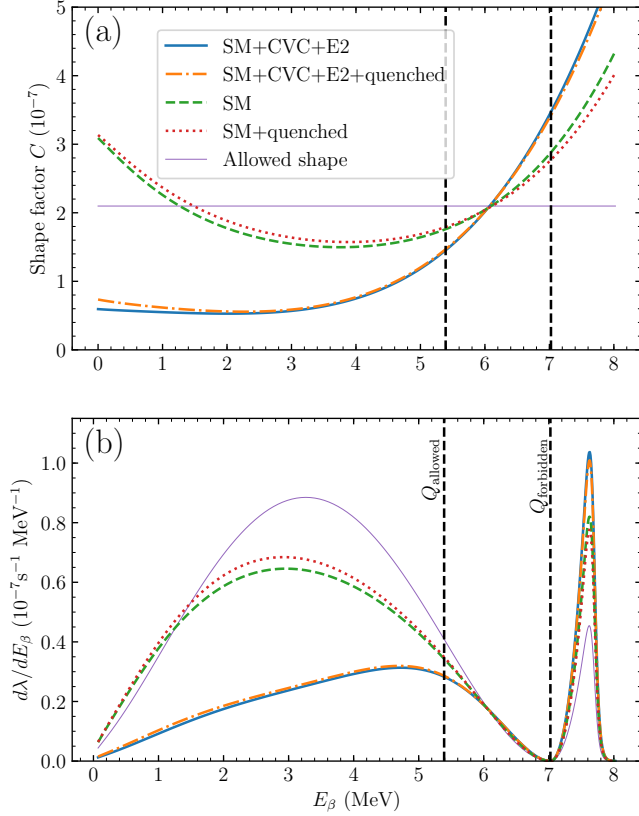


FIG. 15. Normalized shape factors (a) and corresponding  $\beta$ -decay spectra (b) as a function of the electron kinetic energy. The two vertical lines correspond to the  $Q$ -values of the allowed and forbidden transitions, respectively. The experimental data constrains the spectra between these two values. For energies above the  $Q$ -value we show the shape factor for electron capture after dividing by a factor  $\sqrt{5}$  in the upper panel. The lower panel shows spectra of captured electrons for the conditions of temperature,  $\log_{10} T(\text{K}) = 8.6$  and density  $\log_{10} \rho Y_e (\text{g cm}^{-3}) = 9.6$ .

trapolations to lower energies ( $E_\beta < Q_{\text{allowed}}$ ) based on the theoretical shape factors differ substantially, which explains why the inferred branching ratios differ by more than a factor of two, cf. Table III. Similarly, differences can be observed at higher energies in the energy regime relevant to electron capture ( $E_\beta > Q_{\text{forbidden}}$ ). However, due to the relative sharp cut-off of the Fermi-Dirac distribution  $S_e(w, \mu_e)$  we do not need to extrapolate far and the maximal difference is only  $\sim 25\%$ .

In Fig. 16 we show the electron-capture rate on  $^{20}\text{Ne}$  as a function of the density for a temperature of  $\log_{10} T(\text{K}) = 8.6$ . The chosen conditions are representative of those reached during the evolution of degenerate oxygen-neon cores prior to oxygen ignition [12]. The forbidden transition is seen to increase the electron-capture rate by several orders of magnitude in a critical density range compared to the case in which only allowed transitions are considered. The rates computed with the two theoretical models that account for the energy de-

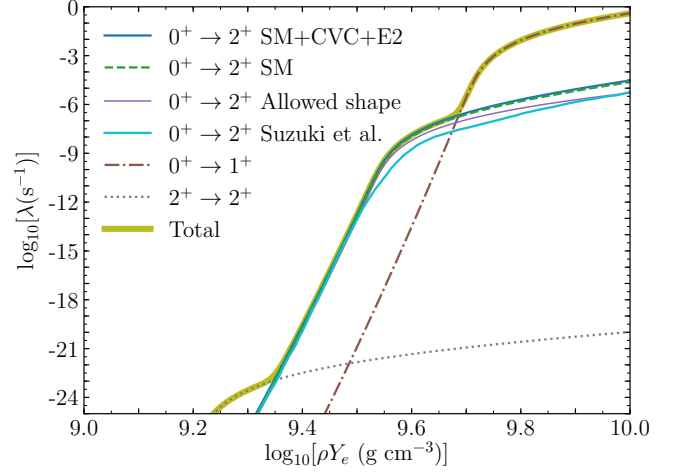


FIG. 16. Electron capture rate on  $^{20}\text{Ne}$  as a function of density at a temperature of  $\log_{10} T(\text{K}) = 8.6$ . We show the contributions of the forbidden transition studied in this work and two allowed transitions: One from the ground state of  $^{20}\text{Ne}$  to the  $1^+$  state in  $^{20}\text{F}$  at 1.056 MeV, and one from the  $2^+$  state of  $^{20}\text{Ne}$  at 1.634 MeV to the ground state of  $^{20}\text{F}$ . The former dominates the rate at densities  $\log_{10} \rho Y_e (\text{g cm}^{-3}) \gtrsim 9.67$ , whereas the latter dominates at  $\log_{10} \rho Y_e (\text{g cm}^{-3}) \lesssim 9.35$ . However, at such densities the rate is so small that it has no influence on the evolution. For reference we also show the forbidden contribution as computed by Suzuki *et al.* [22].

pendence of the forbidden transition differ by less than 25%. Such a small difference has no significant impact on the evolution of degenerate oxygen-neon stellar cores. The rate computed assuming an allowed shape is smaller than the two other rates. The deviation becomes larger at higher densities, but remains within a factor of two in the relevant density range where the forbidden transition dominates over the allowed transition to the  $1^+$  state. The rate determined in Ref. [22] based on a shell-model calculation, which uses the same USDB interaction as in the present work, is substantially smaller than the present rate. The deviation reaches a factor of  $\sim 10$  at densities of  $\log_{10} \rho Y_e (\text{g cm}^{-3}) \sim 9.6$ . The origin of this discrepancy is not clear, but it is likely related to differences in the treatment of the forbidden transition, which lead to substantially different electron spectra (see their Fig. 5).

## VI. DISCUSSION

Shell-model calculations are known to reproduce the strengths of second-forbidden, *unique* transitions in the *sd* shell within a factor of two or better [32, 33]. A similar conclusion was also reached by Ref. [24] regarding the second-forbidden, *non-unique* decay of  $^{36}\text{Cl}$ .

Here, we have shown that for the second-forbidden, non-unique,  $2^+ \rightarrow 0^+$  transition between the ground states of  $^{20}\text{F}$  and  $^{20}\text{Ne}$ , the accuracy is also better than

a factor of two. A purely theoretical calculation overestimates the half-life by a factor of  $\sim 1.6$ , whereas a calculation constrained by the known strength of the analog E2 transition in  $^{20}\text{Ne}$  together with the CVC theory reproduces the experimental half-life to within 10%. It would be of considerable interest to extend this comparison to the much weaker decay of  $^{36}\text{Cl}$  ( $\log ft = 13.321(3)$  [37]), which is the only other known second-forbidden, non-unique transition in the  $sd$  shell. However, this is beyond the scope of the present study and is left for future work.

The  $2^+ \rightarrow 0^+$  transition in the  $\beta$  decay of  $^{20}\text{F}$  was only observed in a narrow energy range near the end point of the  $\beta$  spectrum. This, combined with limited statistics, a modest signal-to-background ratio, and a modest energy resolution, meant that the experimental data did not impose any useful constraints on the shape of the spectrum. Instead, the shape was determined from a combination of theoretical calculations and the known strength of the analog E2 transition in  $^{20}\text{Ne}$ . This led to a branching ratio of  $b_\beta = [0.41 \pm 0.08(\text{stat}) \pm 0.07(\text{sys})] \times 10^{-5}$  and a strength of  $\log ft = 10.89(11)$ . This makes the  $2^+ \rightarrow 0^+$  transition in the  $\beta$  decay of  $^{20}\text{F}$  the second-strongest, second-forbidden, non-unique transition ever measured, with the 27 previously measured transitions having  $\log ft$  values ranging from 10.6 to 14.2 [1].

## VII. CONCLUSION

The second-forbidden, non-unique,  $2^+ \rightarrow 0^+$  ground-state transition in the  $\beta$  decay of  $^{20}\text{F}$  has been observed for the first time. The detection was made possible by the development of a dedicated experimental setup consisting of a Siegbahn-Slätis type intermediate-image magnetic electron transporter combined with a plastic-scintillator telescope. The branching ratio was determined to be  $b_\beta = [0.41 \pm 0.08(\text{stat}) \pm 0.07(\text{sys})] \times 10^{-5}$ , implying  $\log ft = 10.89(11)$ , which makes this the second-strongest, second-forbidden, non-unique  $\beta$  transition ever measured. This remarkable result is supported by our shell-model calculations, which reproduce the experimental strength to within better than a factor of two.

Owing to its large strength, the forbidden transition between the ground state of  $^{20}\text{Ne}$  and  $^{20}\text{F}$  enhances the astrophysical electron-capture rate on  $^{20}\text{Ne}$  by several or-

ders of magnitude at the elevated temperatures and densities achieved in contracting oxygen-neon stellar cores. This has significant impact on the final evolution of such stars as discussed elsewhere. Here, we have shown that the experimental data constrain the astrophysical capture rate to within better than 25%, which is fully sufficient to assess the astrophysical implications.

The experimental data did not impose any useful constraints on the shape of the forbidden  $\beta$  spectrum, which instead was determined based on shell-model calculations and the experimental  $B(E2)$  value of the analog transition in  $^{20}\text{Ne}$ . Future experiments should aim to provide improved constraints on the shape of the forbidden  $\beta$  spectrum, although this will be very challenging.

## ACKNOWLEDGMENTS

We are greatly indebted to the technical staff at the JYFL laboratory and Aarhus University who contributed with their time and expertise to the refurbishment of the spectrometer. We thank F. Lyckegaard for making the  $\text{BaF}_2$  targets, H. Kettunen for preparing the catcher foil, and E. Nacher for providing technical support with the GEANT4 simulations. Finally, we thank C. Matteuzzi, M. Anghinolfi, P. Hansen, R. Julin and T. Kibédi for valuable advice and encouragement in the early phases of the project. This work has been supported by the Academy of Finland under the Finnish Centre of Excellence Programme 2012–2017 (Nuclear and Accelerator Based Physics Research at JYFL) and the Academy of Finland grants No. 275389, 284516 and 312544. DFS and GMP acknowledge the support of the Deutsche Forschungsgemeinschaft (DFG, German Research Foundation) - Projektnummer 279384907 - SFB 1245 “Nuclei: From Fundamental Interactions to Structure and Stars”; and the ChETEC COST action (CA16117), funded by COST (European Cooperation in Science and Technology). This project has been partly supported by the Spanish Ministry MINECO through the grant FPA2015-64969-P and has received funding from the European Union’s Horizon 2020 research and innovation programme under grant agreement No. 654002 (EN-SAR2). OSK acknowledges support from the Villum Foundation through Project No. 10117.

- 
- [1] B. Singh, J. Rodriguez, S. Wong, and J. Tuli, Review of  $\log ft$  values in  $\beta$  decay, *Nuclear Data Sheets* **84**, 487 (1998).
  - [2] G. Martínez-Pinedo, Y. H. Lam, K. Langanke, R. G. T. Zegers, and C. Sullivan, Astrophysical weak-interaction rates for selected  $A = 20$  and  $A = 24$  nuclei, *Phys. Rev. C* **89**, 045806 (2014).
  - [3] J. Schwab, E. Quataert, and L. Bildsten, Thermal runaway during the evolution of ONeMg cores towards accretion-induced collapse, *Monthly Notices of the Royal Astronomical Society* **453**, 1910 (2015).
  - [4] J. Schwab, L. Bildsten, and E. Quataert, The importance of urca-process cooling in accreting one white dwarfs, *Monthly Notices of the Royal Astronomical Society* **472**, 3390 (2017).
  - [5] D. R. Tilley, C. M. Cheves, J. H. Kelley, S. Raman, and H. R. Weller, Energy levels of light nuclei,  $A = 20$ , *Nuclear Physics A* **636**, 249 (1998).
  - [6] E. L. Wilds, Jr., R. H. France III, J. E. McDonald, Z. Zhao, and M. Gai, Upper limits on the first-forbidden

- rank-one  $\beta$  decay of  $^{20}\text{F}$ , Phys. Rev. C **76**, 018501 (2007).
- [7] C. Wong, Beta decay of  $\text{F}^{20}$ , Phys. Rev. **95**, 761 (1954).
- [8] S. S. Glickstein and R. G. Winter, Properties of  $\text{F}^{20}$ , Phys. Rev. **129**, 1281 (1963).
- [9] S. S. Glickstein and R. G. Winter, Properties of  $\text{F}^{20}$ , Phys. Rev. **130**, 2599 (1963).
- [10] F. P. Calaprice and D. E. Alburger, Beta spectrum of  $\text{F}^{20}$ , Phys. Rev. C **17**, 730 (1978).
- [11] The endpoint energies are known to sub-keV precision [5, 38].
- [12] O. S. Kirsebom, S. Jones, D. F. Strömberg, G. Martínez-Pinedo, K. Langanke, F. K. Roepke, B. A. Brown, T. Eronen, H. O. U. Fynbo, M. Hukkanen, A. Idini, A. Jokinen, A. Kankainen, J. Kostensalo, I. Moore, H. Möller, S. T. Ohlmann, H. Penttilä, K. Riisager, S. Rinta-Antila, P. C. Srivastava, J. Suhonen, W. H. Trzaska, and J. Äystö, Discovery of exceptionally strong nuclear transition sheds new light on the fate of intermediate-mass stars, arXiv e-prints (2019), arXiv:1905.09407 [astro-ph.SR].
- [13] J. Ärje, J. Äystö, H. Hyvönen, P. Taskinen, V. Koponen, J. Honkanen, A. Hautojärvi, and K. Vierinen, Submillisecond on-line mass separation of nonvolatile radioactive elements: An application of charge exchange and thermalization processes of primary recoil ions in helium, Phys. Rev. Lett. **54**, 99 (1985).
- [14] I. Moore, T. Eronen, D. Gorelov, J. Hakala, A. Jokinen, A. Kankainen, V. Kolhinen, J. Koponen, H. Penttilä, I. Pohjalainen, M. Reponen, J. Rissanen, A. Saastamoinen, S. Rinta-Antila, V. Sonnenschein, and J. Äystö, Towards commissioning the new IGISOL-4 facility, Nuclear Instruments and Methods in Physics Research Section B: Beam Interactions with Materials and Atoms **317**, Part B, 208 (2013).
- [15] P. Karvonen, I. Moore, T. Sonoda, T. Kessler, H. Penttilä, K. Peräjärvi, P. Ronkanen, and J. Äystö, A sextupole ion beam guide to improve the efficiency and beam quality at igisol, Nuclear Instruments and Methods in Physics Research Section B: Beam Interactions with Materials and Atoms **266**, 4794 (2008).
- [16] H. Slätis and K. Siegbahn, An intermediate image beta-spectrometer of high transmission, Ark. f. Fys. **1**, 339 (1949).
- [17] R. Julin, J. Kantele, J. Kumpulainen, M. Luontama, V. Nieminen, A. Passoja, W. Trzaska, and E. Verho, A setup for spectrometry of high-energy conversion electrons, Nuclear Instruments and Methods in Physics Research Section A: Accelerators, Spectrometers, Detectors and Associated Equipment **270**, 74 (1988).
- [18] P. Jalas, T. Enqvist, V. Isoherranen, J. Joutsenvaara, J. Kutuniva, and P. Kuusiniemi, Callio lab, a new deep underground laboratory in the pyhsalmi mine, Journal of Physics: Conference Series **888**, 012156 (2017).
- [19] H. Behrens and W. Bühring, Nuclear beta decay, Nucl. Phys. A **162**, 111 (1971); *Electron Radial Wave Functions and Nuclear Beta-decay* (Clarendon, Oxford, 1982).
- [20] J. D. Walecka, Semileptonic weak interactions in nuclei, in *Muon Physics*, Vol. II, edited by V. W. Hughes and C. S. Wu (Academic Press, New York, 1975) Section V.4, pp. 113–218.
- [21] T. W. Donnelly and R. P. Peccei, Neutral current effects in nuclei, Phys. Repts. **50**, 1 (1979).
- [22] T. Suzuki, S. Zha, S.-C. Leung, and K. Nomoto, Electron capture rates in  $^{20}\text{Ne}$  for a forbidden transition to the ground state of  $^{20}\text{F}$  relevant to final evolution of high density O-Ne-Mg cores, arXiv e-prints (2019), arXiv:1905.10400 [astro-ph.SR].
- [23] J. C. Hardy and I. S. Towner, Superaligned  $0^+ \rightarrow 0^+$  nuclear  $\beta$  decays: A new survey with precision tests of the conserved vector current hypothesis and the standard model, Phys. Rev. C **79**, 055502 (2009).
- [24] R. Sadler and H. Behrens, Second-forbidden beta-decay and the effect of  $(V + A)$ - and  $S$ -interaction admixtures:  $^{36}\text{Cl}$ , Z. Phys. A **346**, 25 (1993).
- [25] B. A. Brown and W. A. Richter, New “usd” hamiltonians for the  $sd$  shell, Phys. Rev. C **74**, 034315 (2006).
- [26] B. Brown and W. Rae, The shell-model code nushellx@msu, Nuclear Data Sheets **120**, 115 (2014).
- [27] E. U. Condon and G. Shortley, *The Theory of Atomic Spectra* (Cambridge University Press, Cambridge, England, 1951).
- [28] L. C. Biedenharn and M. E. Rose, Theory of angular correlation of nuclear radiations, Rev. Mod. Phys. **25**, 729 (1953).
- [29] G. Fricke, C. Bernhardt, K. Heilig, L. Schaller, L. Schellenberg, E. Shera, and C. Dejager, Nuclear ground state charge radii from electromagnetic interactions, At. Data Nucl. Data Tables **60**, 177 (1995).
- [30] D. Tilley, C. Cheves, J. Kelley, S. Raman, and H. Weller, Energy levels of light nuclei,  $A = 20$ , Nucl. Phys. A **636**, 249 (1998).
- [31] I. S. Towner, Quenching of spin-matrix elements in nuclei, Phys. Repts. **155**, 263 (1987).
- [32] E. K. Warburton, Second-forbidden unique  $\beta$  decays of  $^{10}\text{Be}$ ,  $^{22}\text{Na}$ , and  $^{26}\text{Al}$ , Phys. Rev. C **45**, 463 (1992).
- [33] G. Martínez-Pinedo and P. Vogel, Shell Model Calculation of the  $\beta^-$  and  $\beta^+$  Partial Half-Lives of  $^{54}\text{Mn}$  and Other Unique Second Forbidden  $\beta$  Decays, Phys. Rev. Lett. **81**, 281 (1998).
- [34] J. T. Suhonen, Value of the axial-vector coupling strength in  $\beta$  and  $\beta\beta$  decays: A review, Frontiers in Physics **5**, 55 (2017).
- [35] M. Haaranen, J. Kotila, and J. Suhonen, Spectrum-shape method and the next-to-leading-order terms of the  $\beta$ -decay shape factor, Phys. Rev. C **95**, 024327 (2017).
- [36] A. Juodagalvis, K. Langanke, W. Hix, G. Martínez-Pinedo, and J. Sampaio, Improved estimate of electron capture rates on nuclei during stellar core collapse, Nucl. Phys. A **848**, 454 (2010).
- [37] A. Kriss and D. Hamby, Beta spectroscopy with a large-area avalanche photodiode module and a plastic scintillator, Nuclear Instruments and Methods in Physics Research Section A: Accelerators, Spectrometers, Detectors and Associated Equipment **525**, 553 (2004).
- [38] M. Wang, G. Audi, F. Kondev, W. Huang, S. Naimi, and X. Xu, The AME2016 atomic mass evaluation (ii). Tables, graphs and references, Chinese Physics C **41**, 030003 (2017).